

# THE DYNAMICS AND AFTERGLOW RADIATION OF GAMMA-RAY BURSTS. I. CONSTANT DENSITY MEDIUM

WEIQUN ZHANG AND ANDREW MACFADYEN

Center for Cosmology and Particle Physics, Physics Department, New York University, New York, NY 10003

*Draft version November 2, 2018*

## ABSTRACT

Direct multi-dimensional numerical simulation is the most reliable approach for calculating the fluid dynamics and observational signatures of relativistic jets in gamma-ray bursts (GRBs). We present a two-dimensional relativistic hydrodynamic simulation of a GRB outflow during the afterglow phase, which uses the fifth-order weighted essentially non-oscillatory scheme and adaptive mesh refinement. Initially, the jet has a Lorentz factor of 20. We have followed its evolution up to 150 years. Using the hydrodynamic data, we calculate synchrotron radiation based upon standard afterglow models and compare our results with previous analytic work. We find that the sideways expansion of a relativistic GRB jet is a very slow process and previous analytic works have overestimated its rate. In our computed lightcurves, a very sharp jet break is seen and the post-break lightcurves are steeper than analytic predictions. We find that the jet break in GRB afterglow lightcurves is mainly caused by the *missing* flux when the edge of the jet is observed. The outflow becomes nonrelativistic at the end of the Blandford-McKee phase. But it is still highly nonspherical, and it takes a rather long time for it to become a spherical Sedov-von Neumann-Taylor blast wave. We find that the late-time afterglows become increasingly flatter over time. But we disagree with the common notion that there is a sudden flattening in lightcurves due to the transition into the Sedov-von Neumann-Taylor solution. We have also found that there is a bump in lightcurves at very late times ( $\sim 1000$  days) due to radiation from the counter jet. We speculate that such a counter jet bump might have already been observed in GRB 980703.

*Subject headings:* gamma-rays: bursts – hydrodynamics – methods: numerical – relativity

## 1. INTRODUCTION

In the standard fireball shock model for gamma-ray bursts (GRBs), afterglows are due to synchrotron emission produced during the slowdown of GRB outflows by surrounding media (see e.g., Zhang & Mészáros 2004; Piran 2005; Meszaros 2006; Granot 2007, for recent reviews). The outflows of GRBs are believed to be ultrarelativistic jets. The deceleration of the ultrarelativistic jet-like outflow in the early afterglow stage can be well described by the spherical Blandford-McKee self-similar solution (Blandford & McKee 1976). This is because the relativistic beaming effect makes the material in the jet behave like an angular patch of a spherical blast wave. As it sweeps up the surrounding medium, the jet decelerates and becomes less and less relativistic. Hence the jet-like outflow will eventually expand sideways and become increasingly spherical. Thus the GRB outflow in the very late stages can be described by the Sedov-von Neumann-Taylor non-relativistic self-similar solution. Unfortunately, there is no good analytic solution that can describe the dynamics of the sideways expansion and the transition from the ultrarelativistic phase to nonrelativistic phase.

The evolution of GRB outflows is an extremely important problem. The modeling of observable afterglow emission depends upon the dynamics of the outflow. An achromatic break in afterglow lightcurves is observed in some GRBs (e.g., GRB 990510, Harrison et al. 1999; Stanek et al. 1999). The jet break is an indication that the GRB outflow is jet-like (Rhoads 1999; Sari, Piran, & Halpern 1999). To understand the jet break, we must understand the multi-dimensional dynamics of a relativistic jet. The late-time radio afterglow can be useful for an accurate estimate of the total energy of the GRB outflow (Frail et al. 2000; Berger et al. 2004; Frail et al. 2005). Thus, the understanding of the transition from an ultrarelativistic jet into a Newtonian spherical blast wave is crucial

for correctly interpreting the late-time radio observations.

The dynamics of GRB outflows is a multi-dimensional problem except during the early Blandford-McKee and late Sedov-von Neumann-Taylor phases. Analytic approaches have been attempted to model the sideways expansion based upon the simplified model of the jet as having a top-hat structure as a function of angle during the expansion (Rhoads 1999; Sari et al. 1999; Panaitescu & Mészáros 1999). In these models, the jet experiences significant sideways expansion. To include multidimensional effects in an inexpensive way, Kumar & Granot (2003) reduced the multi-dimensional hydrodynamic equations to one dimension by integrating over the radial profile of the jet. They found little sideways expansion of the jet. However, the validity of these approaches should be tested against full multi-dimensional hydrodynamic simulations, which is certainly the most reliable approach. Unfortunately high-resolution multidimensional relativistic hydrodynamic simulations are very expensive. Thus far, very few multidimensional hydrodynamic simulations have been performed to investigate the dynamics of GRB outflows. Granot et al. (2001) in their pioneering numerical work found that GRB jets experience very little sideways expansion. But their simulation was not long enough to cover the transition into the Sedov-von Neumann-Taylor solution. A recent work by Cannizzo et al. (2004) has also found very little expansion in a different initial setup, but their simulation suffered from severely low resolution.

In this paper, we present a high-resolution relativistic hydrodynamic simulation of the evolution of a GRB outflow during the afterglow phase. The evolution spans from when the Lorentz factor of the jet is 20 until 150 years after the burst. This high-resolution simulation is possible because our code, RAM (Zhang & MacFadyen 2006), is massively parallel, utilizes adaptive mesh refinement (AMR), and uses a fifth-order method. The initial setup and results of the

hydrodynamic simulation will be presented in Section 2. Based upon the hydrodynamic data and standard afterglow models (Sari, Piran, & Narayan 1998; Granot, Piran, & Sari 1999), we have calculated synchrotron emission from the simulated outflow (§ 3). We conclude with further discussions of our results (§ 4).

## 2. DYNAMICS OF GRB OUTFLOWS

### 2.1. Numerical Method and Initial Setup for Hydrodynamic Simulation

The special relativistic hydrodynamic simulation in this paper was performed with the RAM code (Zhang & MacFadyen 2006). RAM utilizes the AMR tools in the FLASH code version 2.3 (Fryxell et al. 2000), which in turn is a modified version of the PARAMESH AMR package (MacNeice et al. 2000). RAM includes several modules to solve the special relativistic hydrodynamics equations. In the simulations in this paper, the fifth-order weighted essentially non-oscillatory (WENO) scheme was used. This scheme has been shown to achieve fifth-order accuracy for smooth flows (Zhang & MacFadyen 2006) and excellent treatment of shocks and contact discontinuities with no tunable numerical parameters.

It is common in hydrodynamic simulations to use a constant gamma-law equation of state (EOS) given by

$$P = (\hat{\gamma} - 1)\rho\epsilon, \quad (1)$$

where  $P$  is pressure,  $\rho$  is mass density,  $\epsilon$  is specific internal energy density and  $\hat{\gamma}$  is the adiabatic index all measured in the fluid rest frame. The adiabatic index can be assumed to be  $4/3$  and  $5/3$  for relativistically hot and cold gas, respectively, but it is usually set as a constant for entire simulations. The problem we studied in this paper, however, involves both hot and cold gas. GRB outflows are relativistically hot at the beginning of the afterglow stage and become Newtonian in terms of both fluid speed and sound speed. The effect of the adiabatic index on GRB afterglows can be quite large. For example, the density jump due to Newtonian strong shock compression is a factor of 4 and 7 for  $\hat{\gamma} = 5/3$  and  $4/3$ , respectively. Hence the constant gamma-law equation of state should be avoided for accurate treatment of afterglow dynamics. The exact equation of state for ideal gas, which works for arbitrary temperature, was given by Sygne (1971). However, it is very expensive to use in numerical simulations because it involves modified Bessel functions of the second and third kinds. To accurately follow the evolution of GRB outflows with a reasonable cost, we used the TM EOS proposed by Mignone, Plewa, & Bodo (2005). This equation of state has the correct asymptotic behavior to  $\hat{\gamma} = 5/3$  and  $4/3$  in the nonrelativistic and relativistic temperature limits, differs with the exact equation of state by less than 4% and can be solved at negligible cost.

Our initial model is derived from the Blandford-McKee solution (Blandford & McKee 1976). Given the energy of the blast wave,  $E_{\text{iso}}$  and the density of the cold surrounding medium,  $\rho_0$ , the blast wave can be fully described by a set of self-similar relations that give the Lorentz factor, pressure and density in the shocked fluid. In our simulation, the energy in the Blandford-McKee solution is set to  $E_{\text{iso}} = 10^{53}$  erg. Note that this energy is not the total energy in the outflow. Instead, it is the compensated energy the outflow would have if it were a spherical blast wave. In the simulation in this paper, we adopted a number density of  $1\text{cm}^{-3}$  for the surrounding medium, which is consistent with GRB afterglow

modeling (e.g., Panaitescu & Kumar 2001, 2002). The surrounding medium is assumed to mainly consist of protons, and it is assumed to be cold,  $P_0 \ll \rho_0$ . Numerically, we set the pressure to  $P_0 = 10^{-10}\rho_0$ , where units in which the speed of light  $c = 1$  are used in the simulation and henceforth in this paper. The hydrodynamic simulation is started at the moment when the Lorentz factor of the fluid just behind the shock is  $\gamma_0 = 20$ . We have run a two-dimensional axisymmetric simulation, in which the half opening angle of the GRB jet is set to be  $\theta_0 = 0.2$  radians. Thus the total energy in the twin jet is  $E_j \simeq 2.0 \times 10^{51}$  erg. According to observations, a total energy of a few times  $10^{51}$  erg is typical (e.g., Frail et al. 2001). A half opening angle of 0.2 radians is also reasonable because it is within the range of half opening angle inferred from observations (e.g., Frail et al. 2001; Panaitescu & Kumar 2001, 2002; Zeh et al. 2006). We chose a slightly large opening angle because of numerical reasons. It is extremely expensive to start our simulations from very early times when the Lorentz factor of the jet is larger, because most of the energy in the Blandford-McKee solution is concentrated in an extremely thin layer behind the shock with a width of  $\sim R/\gamma^2$  in the lab frame, where  $R$  is the radius of the shock. The ‘‘lab’’ frame is the frame in which the central engine is at rest and is equivalent to the observer frame ignoring cosmological factors. In our simulation, we need to resolve the thin structures behind the shock in order to accurately capture the true dynamics. Furthermore, we want the opening angle and Lorentz factor of the jet to satisfy the relation,  $\gamma_0 \gg 1/\theta_0$ , so that the Blandford-McKee solution is still valid for the jet. Our choices of  $\gamma_0 = 20$  and  $\theta_0 = 0.2$  are thus reasonable.

The initial radius of the blast wave at the beginning of the simulation is  $R_0 \simeq 3.8 \times 10^{17}$  cm. The Sedov length for an explosion with an energy of  $E_j \simeq 2.0 \times 10^{51}$  erg into a medium with a density of  $\rho_0 = 1.67 \times 10^{-24}$  g cm $^{-3}$  is

$$l_{\text{SNT}} \equiv \left( \frac{E_j}{(4\pi/3)\rho_0 c^2} \right)^{1/3} \simeq 6.8 \times 10^{17} \text{ cm}. \quad (2)$$

To simulate the evolution of the blast wave up to the Newtonian regime, a large numerical box is necessary. The size of the numerical box for our two-dimensional simulation is  $R_{\text{MAX}} = 1.1 \times 10^{19}$  cm, which is about 16 Sedov lengths. Most of the energy in the blast wave is initially concentrated in a thin layer behind the shock with a width of  $\Delta \sim 10^{15}$  cm in the lab frame. It is thus very challenging to simulate the blast wave over such a large dynamic range in lengthscale even with AMR. At the beginning of the simulation, the thin shell behind the shock occupies a relatively small volume. Thus we can afford to use very high resolution initially. As the blast wave expands, the volume of the thin shell, which contains most of the energy, becomes larger. Thus AMR needs to create increasingly more numerical cells in order to maintain the same high resolution of the structure, making the simulation prohibitively expensive. In our simulation, an algorithm for derefinement of the adaptive mesh suggested by Granot (2007) was used to save computing time. In the FLASH/PARAMESH AMR package, there is a parameter which controls the maximal level of refinement and therefore decides the size of the finest grid, which is usually fixed. We change this parameter over time according to an algorithm which utilizes a nice property of the blast wave that the thin shell which needs to be resolved during the relativistic regime behaves as  $\Delta \sim R/\gamma^2 \sim t^4$ , where  $t$  is the time in the lab

frame. Our algorithm reduces the maximal refinement over time so that roughly the same number of cells are used in the  $r$ -direction to resolve the radially widening shell at different times without suffering from low resolution.

A spherical grid  $(r, \theta)$  with  $0 \leq r \leq 1.1 \times 10^{19}$  cm and  $0 \leq \theta \leq \pi/2$  is employed in our two-dimensional simulation. Initially 16 levels of refinement is used, and the finest cell has a size of  $\Delta r \simeq 5.6 \times 10^{13}$  cm and  $\Delta \theta \simeq 9.6 \times 10^{-5}$ . At this resolution, there are 2086 cells at  $\theta$ -direction inside the jet, and 17 cells inside a shell with a width of  $\Delta_0 = R_0/\gamma_0^2$  behind the shock front. If a uniform grid were used, the total number of cells would have been more than 3 billion in order to achieve the highest resolution provided by AMR. With AMR, less than 7 million cells are needed. In our derefinement algorithm, the maximal level of refinement decreases in response to the change of the shell width until a specified minimal numerical resolution is reached. The minimal resolution is chosen such that AMR uses at least 11 levels.

## 2.2. Results of Two-Dimensional Hydrodynamic Simulation

There are several time scales that are commonly used in the literature. These time scales are measured in the lab frame. Note that they are different from observer times.

- $t_\theta$ : This is the time at which the Lorentz factor behind the shock is equal to  $\gamma = 1/\theta_0$  for a Blandford-McKee solution (Blandford & McKee 1976). It is given by

$$t_\theta \approx 373 E_{\text{iso},53}^{1/3} n_0^{-1/3} \left( \frac{\theta_0}{0.2} \right)^{2/3} \text{ days}, \quad (3)$$

here  $E_{\text{iso},53}$  is the isotropic equivalent energy  $E_{\text{iso}}$  in units of  $10^{53}$  erg and  $n_0$  is density of the medium in units of  $\text{cm}^{-3}$ .

- $t_s$ : Livio & Waxman (2000) argued that the transition from a jet to a spherical self-similar solution takes place over a time  $\Delta t_s \approx R_\theta/c$  where  $R_\theta$  is the jet radius at time  $t_\theta$ . Thus the outflow would become spherical at  $t_s$ , which is given by

$$t_s \approx t_\theta + R_\theta/c \approx 745 E_{\text{iso},53}^{1/3} n_0^{-1/3} \left( \frac{\theta_0}{0.2} \right)^{2/3} \text{ days}. \quad (4)$$

- $t_{\text{SNT}}$ : Livio & Waxman (2000) defined the time  $t_{\text{SNT}}$  as the time at which the shock front moves at the speed of light assuming the blast wave is the Sedov-von Neumann-Taylor solution with an isotropic explosion energy of  $E_j$ . They argued that the GRB outflow becomes subrelativistic and can be described by the Sedov-von Neumann-Taylor solution after the time  $t_{\text{SNT}}$ , which is given by

$$t_{\text{SNT}} \approx 116 \left( \frac{E_j}{2 \times 10^{51} \text{ erg}} \right)^{1/3} n_0^{-1/3} \text{ days}. \quad (5)$$

Note that the time  $t_{\text{SNT}}$  is earlier than the initial time of our simulation  $t_0$ , when the Lorentz factor is  $\gamma_0 = 20$  for a relativistic jet obeying the Blandford-McKee solution. The jet has a Lorentz factor of 29 at  $t_{\text{SNT}}$ . Thus, the GRB outflow at  $t = t_{\text{SNT}}$  is far from being described by the Sedov-von Neumann-Taylor solution. The discrepancy is caused by assuming that the outflow is isotropic.

- $t_{\text{NR}}$ : Piran (2005) argued that the transition from relativistic to Newtonian should take place at  $t_{\text{NR}} = l_{\text{NR}}/c$ , where  $l_{\text{NR}} = (3E_{\text{iso}}/4\pi\rho_0 c^2)^{1/3}$  is the Sedov length assuming that the GRB jet does not expand sideways. After the transition the GRB outflow can be described by the Newtonian Sedov-von Neumann-Taylor solution. The time is given by

$$t_{\text{NR}} \approx 970 E_{\text{iso},53}^{1/3} n_0^{-1/3} \text{ days}. \quad (6)$$

At the time  $t_{\text{NR}}$ , the Lorentz factor behind the shock is 1.2, if one assumes that the GRB does not expand sideways and the Blandford-McKee solution still applies.

It should be emphasized again that the above time scales are measured in the lab frame. They are different from observer times unless the GRB outflow is already nonrelativistic. We will further discuss these time scales in Section 3.1.

Figures 1 and 2 show a series of snapshots of the two-dimensional hydrodynamic simulation. The simulation starts at  $t_0 \simeq 147$  days (measured in the lab frame of the burster) after the initial explosion, and it was run up to 150 years after the explosion. The surrounding medium has a density of  $1.67 \times 10^{-24} \text{ g cm}^{-3}$  and a specific internal energy of  $2.25 \times 10^{-13} \text{ erg cm}^{-3}$ . Initially the relativistic outflow propagates mainly along the radial direction. Later the jet will inevitably undergo sideways expansion. The structure of the flow is very complicated. In Panels (b) and (c) of Figures 1 and 2, we can identify a shock moving sideways, a rarefaction wave propagating towards the jet axis, and a contact discontinuity in between. The contact discontinuity is Kelvin-Helmholtz unstable. There is also a reverse shock inside the rarefaction wave propagating towards the axis. This is caused by the deceleration of the material which moves sideways and sweeps up more and more surrounding medium. It is shown in Panels (b) and (c) of Figures 1 and 2 that the morphology of the GRB outflow at early times consists of a jet cone which moves primarily in the radial direction and a surrounding lobe which moves both radially and sideways. At late times, the GRB outflow becomes egg-like and then increasingly spherical (Panels (d), (e) and (f) of Figures 1 and 2). The nearly vertical Mach stem at the equator is due to the collision of shocks from opposite hemispheres. This feature is unlikely to have direct observational consequences, but it is an indication of the accuracy of the simulation.

What is important for observations is the distribution of the bulk of the energy. Since the jet material near the forward shock front initially moves at nearly the speed of light, very little sideways expansion takes place for the ultrarelativistic material due to relativistic kinematics. Inside the jet, the Lorentz factor decreases radially inwards. The mildly relativistic and Newtonian jet material behind the forward shock front undergoes more sideways expansion as shown in Figures 1 and 2. Also shown in Figures 1 and 2 are snapshots of internal energy density and mass density at  $t = t_{\text{NR}} \approx 970$  days. It should be noted that the GRB outflow at this moment is still highly anisotropic in the angular distribution of energy.

Figure 3 shows the time evolution of the opening angles inside which a certain percentage of the total energy, excluding rest mass energy, resides. At  $t = t_\theta \approx 373$  days, 50%, 90%, 95% and 99% of the total energy are inside an opening angle of 0.14, 0.24, 0.28 and 0.41, respectively. At  $t = t_{\text{NR}} \approx 970$  days, 50%, 90%, 95% and 99% of the total energy is within an opening angle of 0.25, 0.54, 0.63 and 0.77, respectively.

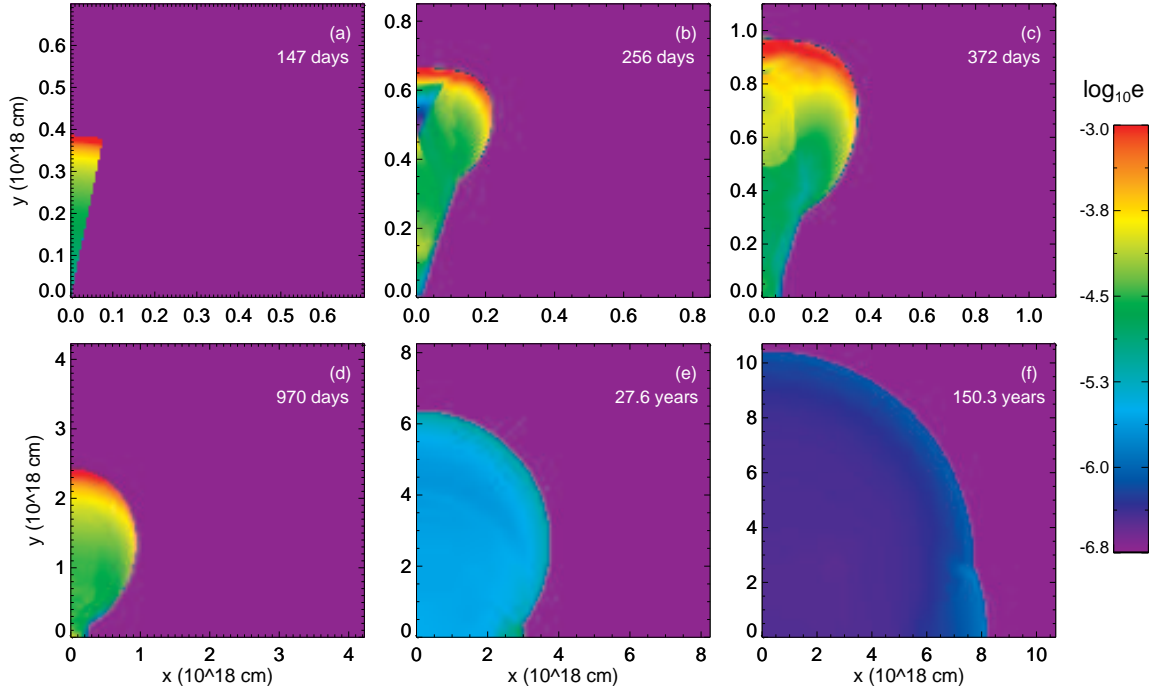


FIG. 1.— Time evolution of the internal energy density in the local rest frame. The internal energy density ( $\text{erg cm}^{-3}$ ) is color coded on a logarithmic scale. Snapshots of the simulation are shown at (a) 147 days, (b) 256 days, (c) 372 days, (d) 970 days, (e) 27.6 years and (f) 150.3 years in the lab frame after the explosion. The beginning of the simulation is at 147 days. Panel (d) shows that the GRB outflow is still highly anisotropic at  $t = t_{\text{NR}} \approx 970$  days. The nearly vertical shock front near the equator in panels (e) and (f) is a Mach stem, which is a result of the shock collision along the equator. The minimal value in the color scale corresponds to  $\leq 10^{-6.8} \text{ erg cm}^{-3}$ . Note that the surrounding medium indeed has an internal energy density of  $\sim 2.25 \times 10^{-13} \text{ erg cm}^{-3}$ .

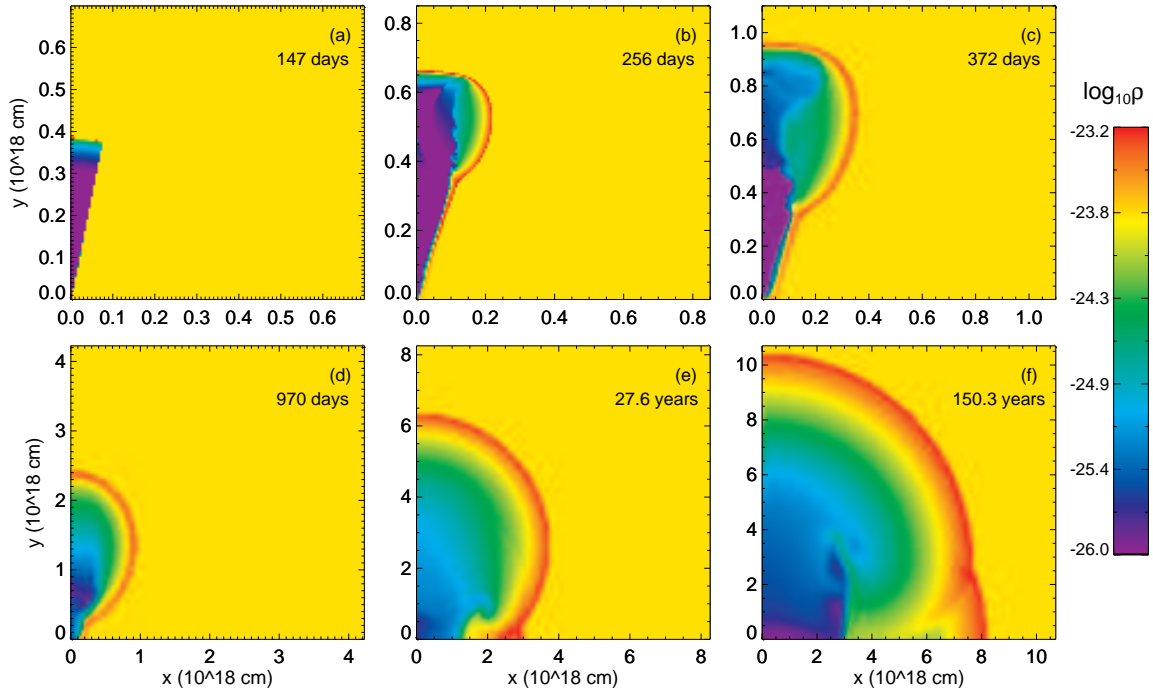


FIG. 2.— Time evolution of the density in the local rest frame. The density ( $\text{g cm}^{-3}$ ) is color coded on a logarithmic scale. Snapshots of the simulation are shown at (a) 147 days, (b) 256 days, (c) 372 days, (d) 970 days, (e) 27.6 years and (f) 150.3 years in the lab frame after the explosion. The beginning of the simulation is at 147 days. Panel (d) shows that the GRB outflow is still highly anisotropic at  $t = t_{\text{NR}} \approx 970$  days. The vortex feature in panels (b) and (c) is an indication of the Kelvin-Helmholtz instability due to velocity shear. The nearly vertical shock front near the equator in panels (e) and (f) is a Mach stem, which is a result of the shock collision along the equator.

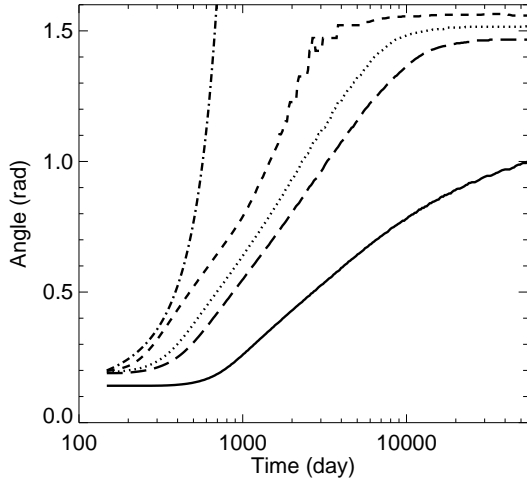


FIG. 3.— Time evolution of the jet opening angle. The opening angles inside which a certain percentage of the total energy, excluding rest mass energy, resides are shown for 50% (solid line), 90% (long dashed line), 95% (dotted line), and 99% (dashed line) of the total energy. Also shown in dash-dotted line is an analytic formula,  $\theta = \theta_0 e^{c(t-t_0)/l_{\text{SNT}}}$ .

At  $t = 20$  years, 50%, 90%, 95% and 99% of the total energy is within an opening angle of 0.72, 1.28, 1.43 and 1.55, respectively. Note that for a spherical blast wave, the opening angles would be 1.05, 1.47, 1.52 and 1.56, for 50%, 90%, 95% and 99% of the total energy, respectively. It is clear that the spreading of energy to large angles happens very slowly. It takes  $\sim 10$ – $20$  years for the jet to be somewhat spherical. The approach to a spherical blast wave and the Sedov-von Neumann-Taylor solution is a very slow process.

The angular distribution of the total energy, excluding rest mass energy at  $t = 0$ ,  $t_\theta \approx 373$  days,  $t_{\text{NR}} \approx 970$  days,  $5t_{\text{NR}} \approx 13$  years and 150 years is shown in Figure 4. The outflow evolves from a jet with an opening angle of  $\theta_0 = 0.2$  into an isotropic blast wave. At  $t = 5t_{\text{NR}} \approx 13$  years, the energy per unit solid angle varies by about an order of magnitude between the axis and the equator. During the evolution, the angular energy distribution is not in any kind of universal profile. In particular, the outflow does not resemble a top-hat jet.

The very little sideways expansion we find is in agreement with the results of previous numerical simulations (Granot et al. 2001; Cannizzo et al. 2004). Figure 3 shows that the opening angle grows logarithmically over time. However, analytic work (Rhoads 1999; Sari, Piran, & Halpern 1999) has predicted that the jet opening angle should grow exponentially,  $\theta \sim e^{c(t-t_0)/l_{\text{SNT}}}$  (Fig. 3). Thus, according to these analytic estimates, the transition from jet-like to spherical-like takes place over practically no time. Why does the jet spread so rapidly in the analytic work compared with that in the numerical simulations? The main reason is that the jet in analytic work is assumed to have an unrealistic top-hat distribution as a function of angle. As it expands sideways, the top-hat jet has more and more working surface, which in turn rapidly decreases the Lorentz factor. Since the speed of the sideways expansion depends upon the Lorentz factor, the sideways expansion of a top-hat jet becomes a runaway process, which grows exponentially. In fact, the jet is far from top-hat during the sideways expansion (Fig. 4). The information of the existence of surrounding medium outside the jet opening angle propagates towards the axis as a rarefaction wave, which moves at the sound speed in the local rest frame. The part of

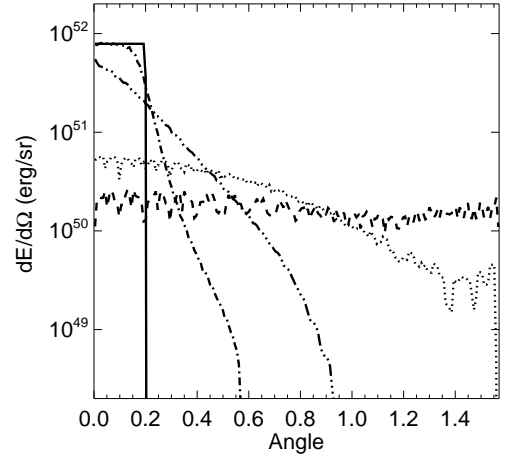


FIG. 4.— Angular distribution of energy. Different lines are for different times:  $t = 0$  (solid line),  $t_\theta \approx 373$  days (dash-dotted line),  $t_{\text{NR}} \approx 970$  days (dash dot dot line),  $5t_{\text{NR}} \approx 13$  years (dotted line) and 150 years (dashed line).

the jet that the rarefaction has not reached will behave exactly like a spherical outflow and continue to expand radially. The part of the jet that is affected laterally by the jet edge is inside a rarefaction wave, which has a more complicated angular profile than a top-hat. Moreover, the reverse shock which appears in the early stages further slows down the sideways expansion. Can numerical simulations underestimate the rate of sideways expansion? We believe that it is unlikely. In fact, numerical simulations tend to overestimate the rate of sideways expansion of relativistically moving material due to the inevitable numerical viscosity (Zhang & MacFadyen 2006). Also the Blandford-McKee solution is very challenging for numerical simulations due to its extremely thin structure behind the shock. The Lorentz factor of the material just behind the shock tends to be lower than the analytic Blandford-McKee solution (Fig. 5). This will also increase the rate of sideways expansion numerically. Hence, we conclude that the runaway lateral expansion derived in the analytic work does not exist in reality and the sideways expansion is a slow process.

Figure 5 shows the time evolution of various properties of the fluid just behind the forward shock: the position of the shock front, the product of the Lorentz factor and radial velocity, and the internal energy density at various angles:  $\theta = 0$ ,  $0.19$ , and  $\pi/4$ . Also shown are the Blandford-McKee solution and Sedov-von Neumann-Taylor solution for comparison. It is shown that the outflow can be approximately described by the Blandford-McKee solution at early times ( $t < t_{\text{NR}} \approx 970$  days) and the Sedov-von Neumann-Taylor solution at late times ( $t > 5t_{\text{NR}} \approx 5000$  days). And the transition takes place over a period of  $\sim 4t_{\text{NR}}$ . It is striking that the Blandford-McKee solution is valid for the material near the jet axis until the time when the Lorentz factor decreases almost to 1. Note that the assumption of ultrarelativistic velocity upon which the Blandford-McKee solution is based has become invalid before that time. It should also be noted that even with 16 levels of mesh refinement, the simulation still suffers from insufficient resolution at early times.

The results of our hydrodynamic simulation are summarized as follows: (1) The initial condition of the jet is described by the Blandford-McKee solution; (2) The jet slows

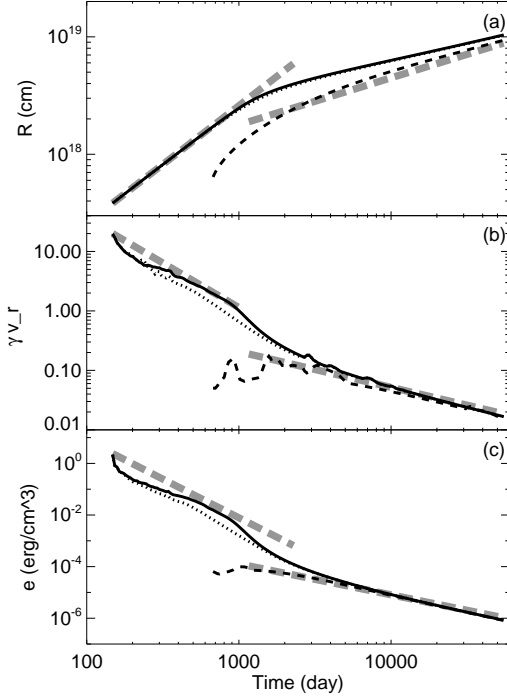


FIG. 5.— Properties of the fluid just behind the forward shock as a function of time. The position of the forward shock, the product of the Lorentz factor and radial velocity, and internal energy density are plotted in Panels (a) (*top*), (b) (*middle*), and (c) (*bottom*), respectively. Properties at three different angles are shown: (1)  $\theta = 0$  (*solid lines*), (2)  $\theta = 0.19$  (*dotted lines*), and (3)  $\theta = \pi/4$  (*dashed lines*). In Panel (b), the unit for velocity is the speed of light. The Blandford-McKee solution and Sedov-von Neumann-Taylor solution are also shown in thick gray dashed lines. In Panel (b), instead of the product of the Lorentz factor and velocity, the Lorentz factor and velocity are plotted, for the Blandford-McKee solution and Sedov-von Neumann-Taylor solution, respectively.

down as it sweeps up the surrounding medium; (3) At  $t \sim t_\theta$ , the jet starts to undergo sideways expansion, but at a rate much slower than the exponential growth predicted by analytic work; (4) The jet becomes nonrelativistic and the Blandford-McKee solution breaks down at  $t \sim t_{NR}$ ; (5) The outflow becomes more and more spherical and undergoes a *slow* transition into the Sedov-von Neumann-Taylor solution; (6) After  $t \sim 5t_{NR}$ , the outflow is close to spherical and can be described by the Newtonian Sedov-von Neumann-Taylor solution.

### 3. AFTERGLOW RADIATION OF GRBS

We now calculate the afterglow radiation of GRBs using the data from our two-dimensional special relativistic hydrodynamic simulation.

#### 3.1. Frames and Times

Two frames are involved in the hydrodynamic simulation (§ 2.2): the local rest frame of a fluid element and the lab frame of the GRB central engine. The measurements of spacetime in the above two frames satisfy the Lorentz transformation. For an observer on the earth, there is an additional frame: the observer frame<sup>1</sup>. If a photon is emitted at time  $t$

<sup>1</sup> The observer frame is the same inertial frame as the lab frame if cosmological effects are neglected (Zhang & Mészáros 2004).

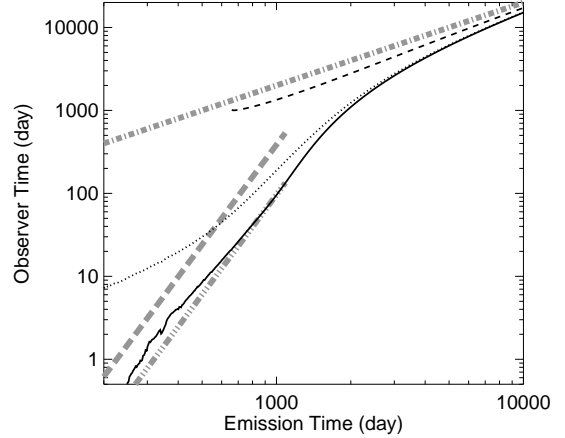


FIG. 6.— Observer time vs. Emission time. The results for fluid elements just behind the shock at various angles are shown:  $\theta = 0$  (*solid line*),  $0.19$  (*dotted line*), and  $\pi/4$  (*dashed line*). The relations  $t_\oplus = (1+z)t/4\gamma^2$  (*long dashed gray line*) and  $t_\oplus = (1+z)t/16\gamma^2$  (*dash dot dot gray line*) are plotted for comparison. Here,  $\gamma$  is assumed to obey the Blandford-McKee solution, and the cosmological redshift is set to  $z = 1$ . Also plotted is  $t_\oplus = (1+z)t$  (*dash-dotted gray line*).

and position  $\vec{r}$  in the lab frame, an observer will receive it at

$$t_\oplus = (1+z)\left(t - \frac{\vec{r} \cdot \vec{n}}{c}\right) \quad (7)$$

after the main burst. Here,  $z$  is the redshift of the GRB, and  $\vec{n}$  is the unit vector pointing from the burster to the earth. Clearly, photons received by the observer at a given time are emitted by different regions of the GRB outflow at different times. However, the emission is mostly from a very small region if the outflow is relativistic. Therefore, a simple relation is often used in analytic work for the emission time and observer time. For a GRB outflow in the relativistic phase, the two times satisfy

$$t_\oplus \approx (1+z)\frac{t}{4\gamma^2}, \quad (8)$$

here  $\gamma$  is the Lorentz factor of the fluid just behind the shock, which is described by the Blandford-McKee solution. The factor of 4 in the denominator of Equation 8 is due to the effect that “typical” photons seen by an observer are emitted from off-axis regions (e.g., Waxman 1997a). When the velocity of the outflow is Newtonian (i.e.,  $v \ll c$ ), the relation is simply

$$t_\oplus \approx (1+z)t. \quad (9)$$

There is, however, no good analytic relation for the transrelativistic phase.

Our numerical approach has the advantage of treating the various times accurately. Figure 6 shows the observer time versus emission time for fluid elements just behind the shock at various angles. Analytic relations are also plotted for comparison. We have discussed various timescales in § 2.2, including  $t_\theta$ ,  $t_s$ ,  $t_{SNT}$  and  $t_{NR}$  (Eqs. 3, 4, 5 and 6). All these timescales are measured in the lab frame. A good approximation is that Eq. 8 is valid for  $t_\theta$ . The time  $t_s$  consists of two parts (Eq. 4). Since the outflow is relativistic before  $t_\theta$  and is then assumed to become Newtonian very quickly due to the sideways expansion, Livio & Waxman (2000) argued that the GRB outflow will become spherical at  $t_{s,\oplus} \sim (1+z)R_\theta/c \sim 372(1+z)E_{iso,53}^{1/3}t_0^{-1/3}(\theta_0/0.2)^{2/3}$  days. The time

$t_{\text{NR},\oplus} \sim (1+z)t_{\text{NR}} \sim 970(1+z)E_{\text{iso},53}^{1/3}n_0^{-1/3}$  days is also often assumed to be the beginning of the Sedov-von Neumann-Taylor phase (e.g., Piran 2005). But it is clearly shown in Figure 6 that the relation  $t_{\oplus} = (1+z)t$  cannot be used at times  $t_s$  and  $t_{\text{NR}}$ . It would be a mistake to treat them as the observer times (after a cosmological redshift correction.) Another mistake is that the outflow at these times is neither spherical nor Sedov-von Neumann-Taylor as we have shown in § 2.2. The transition to the spherical Sedov-von Neumann-Taylor solution takes place over a rather long period ( $\sim 5t_{\text{NR}}$ ) in the lab frame. But, it turns out that the two mistakes somewhat compensate each other. At  $t_{\oplus} = (1+z)t_{\text{NR}}$ , the observed radiation is emitted by nonrelativistic material, which is undergoing the transition into the spherical Sedov-von Neumann-Taylor phase. However,  $(1+z)t_{\text{SNT}} \approx 116(1+z)(E_j/2 \times 10^{51} \text{ erg})^{1/3}n_0^{-1/3}$  days is certainly inappropriate as the observer time for the beginning of either the nonrelativistic phase or the Sedov-von Neumann-Taylor phase.

### 3.2. Standard Afterglow Model

Our calculation of the radiation is based upon the standard external shock model for GRB afterglows (Meszaros & Rees 1997; Wijers et al. 1997; Waxman 1997b,a; Sari et al. 1998). We use the formalism introduced by Granot et al. (1999), which works nicely with data from numerical simulations. A large number of data dumps from the hydrodynamic simulation are stored. The numerical GRB outflow consists of many small fluid elements  $\Delta V = 2\pi r^2 \sin\theta \Delta r \Delta\theta$  at a discrete set of lab times. The velocity, number density and internal energy density of each fluid element is known at each lab time. A fluid element is assumed to exist over a period of  $\Delta t$  depending upon the interval between dumps. The observed flux density at  $t_{\oplus}$  given by Eq. 7 over a period of  $\Delta t_{\oplus} = (1+z)\Delta t$  due to radiation emitted by the fluid element is given by,

$$\Delta F(\nu_{\oplus}, t_{\oplus}) = \frac{1+z}{4\pi d_L^2} \frac{P'(\nu')}{\gamma^2(1-\vec{\beta} \cdot \vec{n})^2} \Delta V, \quad (10)$$

here  $d_L$  is the luminosity distance,  $\gamma$  is the Lorentz factor,  $\vec{\beta}$  is the dimensionless velocity of the fluid element, and  $P'(\nu')$  is the emitted energy per unit volume per unit frequency per unit time measured in the fluid rest frame, where the frequency  $\nu'$  is also measured in the fluid rest frame. The frequencies measured in the fluid rest frame and observed on the earth are related by <sup>2</sup>

$$\nu' = (1+z)\gamma(1-\vec{\beta} \cdot \vec{n})\nu_{\oplus}. \quad (11)$$

The total observed flux density as a function of frequency and observer time,  $F(\nu_{\oplus}, t_{\oplus})$ , can be calculated by combining  $\Delta F(\nu_{\oplus}, t_{\oplus})$  over all the fluid elements at all discretized times.

We consider synchrotron emission, but ignore synchrotron self-absorption and inverse Compton scattering, for the sake of simplicity. To compute synchrotron emission of a fluid element with a number density  $n$  and an internal energy density  $e$ , we use the standard approach of assuming that  $e_e = \epsilon_e e$  and  $e_B = \epsilon_B e$ , here  $e_e$  is the energy density of radiation emitting electrons,  $e_B$  is the energy density of the magnetic field, and  $\epsilon_e$  and  $\epsilon_B$  are two parameters. A power-law distribution is assumed for the radiation emitting electrons:  $N(\gamma_e) \sim \gamma_e^{-p}$ , where  $\gamma_e$  is the Lorentz factor of electrons, and  $p = 2.5$  is a

constant parameter. We follow the work of Sari et al. (1998) for calculating synchrotron emission. For our purposes, it is sometimes more convenient to use the lab frame time. We have taken into account the effect of electron cooling on the spectral power of synchrotron emission. The critical value of the Lorentz factor of electrons is computed using

$$\gamma_c = \frac{3m_e c \gamma}{4\sigma_T e_B t}, \quad (12)$$

here  $m_e$  is the mass of an electron,  $\sigma_T$  is the Thompson cross section,  $\gamma$  is the Lorentz factor of the fluid element, and  $t$  is the time in the lab frame. The spectral power of synchrotron emission is assumed to be a broken power-law with three segments separated by  $\nu_c$ , the cooling frequency, and  $\nu_m$ , the typical frequency of electrons with the minimal Lorentz factor. Assuming that the outflow obeys the Blandford-McKee solution and the emission time and observer time are related by Eq. 8, the two break frequencies in the observer frame are given by<sup>3</sup>

$$\begin{aligned} \nu_{c,\oplus} &= 1.8 \times 10^{11} (1+z)^{-1} \epsilon_B^{-3/2} n_0^{-3/2} \left( \frac{t}{147 \text{ days}} \right)^{-2} \text{ Hz} \\ &= 5.3 \times 10^{10} (1+z)^{-1/2} \epsilon_B^{-3/2} E_{\text{iso},53}^{-1/2} n_0^{-1} t_{\oplus,d}^{-1/2} \text{ Hz} \end{aligned} \quad (13)$$

and

$$\begin{aligned} \nu_{m,\oplus} &= 6.7 \times 10^{16} (1+z)^{-1} \epsilon_B^{1/2} \epsilon_e^2 E_{\text{iso},53}^2 n_0^{-3/2} \left( \frac{t}{147 \text{ days}} \right)^{-6} \text{ Hz} \\ &= 1.8 \times 10^{15} (1+z)^{1/2} \epsilon_B^{1/2} \epsilon_e^2 E_{\text{iso},53}^{1/2} t_{\oplus,d}^{-3/2} \text{ Hz}, \end{aligned} \quad (14)$$

here  $t_{\oplus,d}$  is the observer time in units of days. The peak flux density is given by

$$F_{\nu,\text{max}} = 970(1+z)\epsilon_B^{1/2} E_{\text{iso},53} n_0^{1/2} d_{L,28}^{-2} \text{ mJy}. \quad (15)$$

Here, a factor of 0.88 was added to the expression for  $F_{\nu,\text{max}}$  (Eq. 11 in Sari et al. 1998) to reflect the fact that the synchrotron emission at the peak frequency has a smoothly curved shape rather than a broken power-law shape (Granot et al. 1999). The two break frequencies become equal to the critical frequency

$$\nu_{t,\oplus} = 2.9 \times 10^8 (1+z)^{-1} \epsilon_B^{-5/2} \epsilon_e^{-1} E_{\text{iso},53}^{-1} n_0^{-3/2} \text{ Hz} \quad (16)$$

at

$$t_t = 3.6 \times 10^3 \epsilon_B^{1/2} \epsilon_e^{1/2} E_{\text{iso},53}^{1/2} \text{ days}, \quad (17)$$

which corresponds to

$$t_{t,\oplus} = 3.4 \times 10^4 (1+z)\epsilon_B^2 \epsilon_e^2 E_{\text{iso},53} n_0 \text{ days}. \quad (18)$$

In the calculation present in this paper, we assume that  $\epsilon_e = 0.1$ ,  $\epsilon_B = 0.1$ , and the GRB is located at  $z = 1$ . At the beginning of the simulation,  $t_0 = 147$  days, the two break frequencies are  $\nu_{c0,\oplus} = 2.8 \times 10^{12} \text{ Hz}$  and  $\nu_{m0,\oplus} = 1.1 \times 10^{14} \text{ Hz}$ . Hence the GRB outflow is initially in the fast cooling regime. The transition from the fast cooling to slow cooling regime takes place at 360 days in the lab frame, which corresponds to 6.8 days for the observer, and the transition frequency is  $\nu_{t,\oplus} = 4.6 \times 10^{11} \text{ Hz}$ .

<sup>2</sup> There is a typo in Eq. 4 of Granot et al. (1999). There should be a factor of  $1+z$  in the first argument of  $P'$ .

<sup>3</sup> Our Eq. 13 for  $\nu_c$  is 16 times smaller than Eq. 11 in Sari et al. (1998) due to a factor of 4 difference in the expression for  $\gamma_c$  between our Eq.12 and Eq. 6 in Sari et al. (1998).



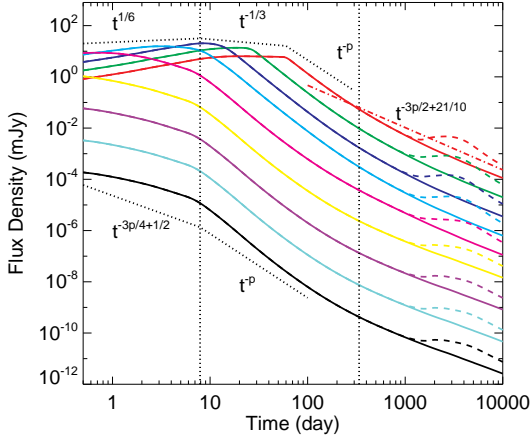


FIG. 7.— Multi-frequency lightcurves. The afterglow radiation from the forward jet is shown in solid lines, whereas the radiation from both the forward jet and counterjet is shown in dashed lines. Flux density for various frequencies from radio to X-ray is plotted:  $10^9$  (red),  $10^{10}$  (green),  $10^{11}$  (blue),  $10^{12}$  (cyan),  $10^{13}$  (magenta),  $10^{14}$  (yellow),  $10^{15}$  (purple),  $10^{16}$  (aqua), and  $10^{17}$  Hz (black). Plotted in black dotted lines for comparison are lightcurves with slopes from Sari et al. (1999); Rhoads (1999). It should be noted that these analytic lines are arbitrary in magnitude. An analytic lightcurve for frequency at 1 GHz in the nonrelativistic phase (Fraai et al. 2000; Livio & Waxman 2000) is also plotted in red dash-dotted line. The vertical dotted lines are at 7.9 and 340 days.

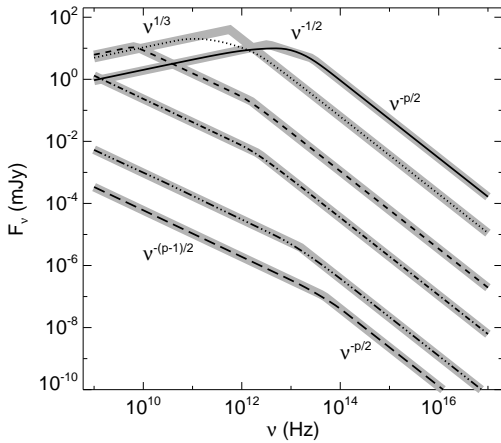


FIG. 8.— Spectra at various times. Thin black lines are results of our calculation for different times:  $t_{\oplus} = 0.6$  (solid line), 8 (dotted line), 30 (dashed line), 100 (dash-dotted), 1000 (dash dot dot line), and 10000 days (long dash line). Thick gray lines are fitted using analytic formulae for synchrotron emission from nonthermal electrons with a power-law distribution. (Sari et al. 1998).

### 3.3. Results of Afterglow Calculation

A large amount of data from the hydrodynamic simulation needs to be stored for the calculation of afterglow radiation observed on the earth. Without an adequate number of data dumps, the afterglow calculation will not be very accurate. However, an unnecessary amount of data would be generated if we simply dumped data equally spaced in time because of the power-law time dependence of the blast wave. For our simulation, 3000 data dumps equally spaced in logarithmic time have been made. To test whether 3000 dumps is sufficient. We have performed low-resolution runs with 5000 dumps. We found almost no difference in the results of the

afterglow calculation between using all 5000 dumps and using only 3000 of the 5000 dumps. Therefore we conclude that the frequency of dumping data is sufficient.

In this calculation, we use a cosmology with  $H_0 = 71 \text{ km s}^{-1} \text{ Mpc}^{-1}$ ,  $\Omega_M = 0.27$ , and  $\Omega_{\Lambda} = 0.73$ . Using the hydrodynamic data (§ 2.2) and the standard afterglow model (§ 3.2), we have calculated multi-frequency lightcurves (Fig. 7). The calculated flux density covers a wide frequency range: from  $10^9$  Hz (radio) to  $10^{17}$  Hz (X-ray), and a wide range of observer time: from 0.5 day after the burst to  $\sim 27$  years. The spectra at various times are shown in Figure 8.

#### 3.3.1. Jet Break

It is shown in Figure 7 that there is an achromatic break in the lightcurves at  $\sim 8$  days. Using the analytic work of Sari et al. (1999), we can estimate that the jet break happens at  $t_j \approx 3.5(1+z)E_{\text{iso},53}^{1/3}n_0^{-1/3}(\theta_0/0.2)^{8/3}$  days  $\approx 7.0$  days. However, we believe that while they happened to get the correct answer, their treatment of the sideways expansion was flawed (§ 2.2). Furthermore, there is ambiguity in the relation between the emission time and the observer time. The jet break would still exist even if there is no sideways expansion (Mészáros & Rees 1999; Panaitescu & Mészáros 1999; Granot & Kumar 2003). Once the observer sees the edge of the jet, the observed flux will decrease rapidly due to the obvious difference between a spherical blast wave and a jet and the sideways expansion will help decrease the flux. It is usually thought that the break due to missing flux would be shallower than the break due to sideways expansion. This is incorrect because the image of a GRB afterglow is limb-brightened (Granot et al. 1999). We will discuss this in more detail later in this section. According to this line of argument, we can also estimate the jet break time. For the sake of simplicity, one can think that the information about the existence of an edge propagates towards the axis as a rarefaction wave, which moves at the local sound speed  $c_s$ . Therefore, the angle of the head of the rarefaction wave is  $\theta_{\text{RF}} \sim \theta_0 - \gamma^{-1}c_s/c \sim \theta_0 - \gamma^{-1}/\sqrt{3}$ . An observer on the axis will see the rarefaction when  $\gamma \sim 1/\theta_{\text{RF}} \sim \theta_0^{-1}(1+1/\sqrt{3})$ . The jet break time is around the moment when that happens. This leads to

$$t_j \approx 3.9(1+z)E_{\text{iso},53}^{1/3}n_0^{-1/3}\left(\frac{\theta_0}{0.2}\right)^{8/3} \text{ days}, \quad (19)$$

where  $E_{\text{iso},53}$  is the isotropic equivalent energy in units of  $10^{53}$  erg.

The analytic results of Sari et al. (1998, 1999); Rhoads (1999) are also plotted in Figure 7 for comparison. For example, they predicted that the flux density at high frequencies ( $\nu_{\oplus} > \nu_{m,\oplus}$ ) evolves as

$$F_{\nu} \propto t_{\oplus}^{-p}. \quad (20)$$

Note that in our model the transition from the fast cooling to the slow cooling regime takes place at  $\sim 7$  days (§ 3.2; Fig. 8), which is roughly the same time as the jet break. For  $\nu_{\oplus} < 10^{12}$  Hz, the flux density evolves as  $\sim t_{\oplus}^{1/2}$  before the jet break, deviating from the analytic result that it should evolve as  $\sim t_{\oplus}^{1/6}$  (Sari et al. 1998) probably due to still insufficient resolution for ultrarelativistic material, and then becomes essentially flat until the frequency is above the typical frequency  $\nu_{m,\oplus}$ . Then the flux density is slightly steeper than  $t_{\oplus}^{-p}$ . For  $\nu_{t,\oplus} \sim 10^{12}$



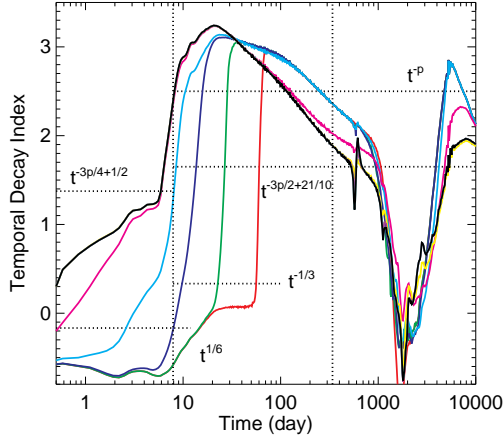


FIG. 9.— Temporal decay index as a function of time. Assuming  $F_\nu \sim t^{-\alpha}$ , the temporal decay index  $\alpha$  for various frequencies from radio to X-ray is plotted:  $10^9$  (red),  $10^{10}$  (green),  $10^{11}$  (blue),  $10^{12}$  (cyan),  $10^{13}$  (magenta),  $10^{14}$  (yellow),  $10^{15}$  (purple),  $10^{16}$  (aqua), and  $10^{17}$  Hz (black). Note that the indices for the last four lines (from  $10^{14}$  to  $10^{17}$ ) are almost identical. Also plotted for comparison are analytic results of Sari et al. (1999); Frail et al. (2000). The vertical dotted lines are at 7.9 and 340 days.

Hz, the flux density is essentially flat before the jet break, and is steeper than  $t_\oplus^{-p}$  afterwards. For  $\nu_\oplus > 10^{12}$ , the flux density is flatter than  $t_\oplus^{-3p/4+1/2}$  before the jet break, probably also due to still insufficient resolution for ultrarelativistic material ( $\gamma > 10$ ). Then it becomes much steeper than  $t_\oplus^{-p}$ .

The most notable difference between our simulation results and previous analytic results (Sari et al. 1999; Rhoads 1999) is the sharpness of the jet break in our results. At radio frequencies, the post-break lightcurves after the spectral break can be fitted approximately by  $\sim t_\oplus^{-p}$ . But at optical and X-ray frequencies, the post-break lightcurves can no longer be fitted by a simple power-law. If the power-law form  $t^{-\alpha}$  is used for the fit, the lightcurves have a varying temporal decay index as shown in Figure 9. The temporal indices for  $\nu_\oplus = 10^{14}$  Hz and above are almost identical as expected for frequencies above both the cooling frequency  $\nu_{c,\oplus}$  and typical frequency  $\nu_{m,\oplus}$ . Note that a statistical study of pre-Swift bursts (Zeh et al. 2006) found that the post-break temporal decay index was in the range of 1.30–3.03. It is shown in Figure 9 that the post-break temporal decay index can increase to  $\sim 3$  and then decreases to below the electron power-law index  $p$ . This is consistent with the argument that jet break is caused by the *missing* flux outside the jet opening angle. It should be noted that photons received by an observer at a given observer time are not emitted at the same time in the lab frame because of the difference in light travel time for different parts of the outflow. It takes longer for photons emitted from off-axis parts of the jet to reach the observer than photons emitted on the axis at the same lab frame time. Thus, at a given observer time, the radiation from the off-axis part of the jet was emitted earlier when the jet energy density (which is decreasing as the jet decelerates) was higher and is brighter than that from the axis. In other words, the image of a GRB afterglow is limb-brightened (Granot et al. 1999). Once the edge of the jet is seen by the observer, the flux density will decrease rapidly. Since the *missing* flux is brighter, the temporal decay index will overshoot after the jet break (see also Granot 2007). Because the afterglow image is more limb-

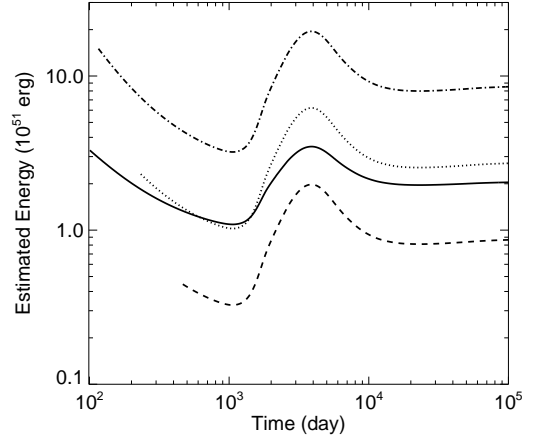


FIG. 10.— Estimated energy as a function of observer time. With observed flux density at  $\nu_\oplus = 1$  GHz, one can estimate the total energy of the GRB outflow using Eq. 23 (solid line) or Eq. 22. The latter estimate requires an estimate of the Sedov-von Neumann-Taylor time  $t_{\text{SNT}}$ . Three different values for  $t_{\text{SNT}}$  are used: 116 (dotted line), 232 (dashed line), and 58 days (dash-dotted line). The true energy is  $2 \times 10^{51}$  erg.

brightened for frequencies above the cooling frequency than below (Granot et al. 1999), the overshooting is more prominent at higher frequencies than lower frequencies.

The spectra at various times are shown in Figure 8. They can be fit by broken power-law curves as expected. This confirms the analytic analysis in § 3.2. The outflow is initially in the fast cooling regime. The two break frequencies become equal at  $\sim 8$  days. Then the slow cooling regime is entered. The typical frequency  $\nu_{m,\oplus}$  continues to decrease over time. However the cooling frequency  $\nu_{c,\oplus}$  increases slowly from  $\sim 10^{12}$  Hz at 8 days to  $\sim 10^{14}$  Hz at 10,000 days.

### 3.3.2. Nonrelativistic Regime

We have discussed in § 2.2 that  $t_{\text{NR}}$  in the lab frame marks the beginning of nonrelativistic regime. Using the relation  $t_\oplus \sim (1+z)t/4\gamma^2$ , we can obtain

$$t_{\text{NR},\oplus} \approx 170(1+z)E_{\text{iso},53}^{1/3}n_0^{-1/3} \text{ days}. \quad (21)$$

When the GRB outflow becomes a Sedov-von Neumann-Taylor blast wave at late times, the lightcurve will become flatter (Dai & Lu 1999; Frail et al. 2000; Huang & Cheng 2003). At late times, the radio frequency is typically in between  $\nu_{m,\oplus}$  and  $\nu_{c,\oplus}$  (Fig. 8). The radio lightcurve in the Sedov-von Neumann-Taylor phase evolves as (Frail et al. 2000; Livio & Waxman 2000)

$$F_\nu \approx 0.2(1+z)^{(3-p)/2} \left(\frac{\epsilon_e}{0.1}\right) \left(\frac{\epsilon_B}{0.1}\right)^{3/4} n_0^{3/4} E_{j,51} d_{L,28}^{-2} \nu_{\text{GHz}}^{-(p-1)/2} \times \left(\frac{t_\oplus}{t_{\text{SNT}}(1+z)}\right)^{(21-15p)/10} \text{ mJy}, \quad (22)$$

here  $d_{L,28}$  is the luminosity distance in units of  $10^{28}$  cm, and  $\nu_{\text{GHz}}$  is frequency in units of GHz.

It should be emphasized that the GRB outflow at  $t_{\text{NR}}$  cannot be described by the Sedov-von Neumann-Taylor solution yet because it is still highly nonspherical. In fact, it does not become approximately spherical until  $\sim 5t_{\text{NR}}$ . Since the transition from relativistic to nonrelativistic flow is very smooth (§ 2.2), it is reasonable that the lightcurves at late times be-

come flat gradually (Figs. 7 and 9). There are no sharp breaks in them except the bumps from the counter jet at very late times. According to Frail et al. (2000); Berger et al. (2004); Frail et al. (2005) since the lightcurve can be observed months or even years after the burst when the outflow is putatively a spherical Sedov-von Neumann-Taylor blast wave, the radio afterglow would allow for an accurate estimate of the total energy of the GRB outflow. They used the flattening present in the observed radio afterglow lightcurves to estimate  $t_{\text{SNT}}$ , and performed calorimetric analysis of the explosions. However, there is no sharp transition in the lightcurves calculated from our simulation (Fig. 7). It would therefore be very inaccurate to determine  $t_{\text{SNT}}$  from the rather smooth late-time afterglow. It is shown in Figure 10 that the estimated energy using Eq. 22 could have an order of magnitude difference if the estimated  $t_{\text{SNT}}$  varies by a factor of 4. Here, other parameters such as  $\epsilon_e$ ,  $\epsilon_B$ ,  $p$  and  $n_0$  are assumed to be known. The emission from the counter jet can be observed at late times too. This causes a bump in the lightcurves (Fig. 7). Eq. 22 and our calculation do not match very well until  $t_{\oplus} \sim 50(1+z)t_{\text{SNT}} \sim 10^4$  days. Fortunately, by substituting Eq. 5 into Eq. 22, we can obtain an equation without  $t_{\text{SNT}}$ ,

$$F_{\nu} \approx 0.16(1+z)^{(3-p)/2} \left(\frac{\epsilon_e}{0.1}\right) \left(\frac{\epsilon_B}{0.1}\right)^{3/4} n_0^{(29-10p)/20} E_{j,51}^{(5p+3)/10} \\ \times d_{L,28}^{-2} \nu_{\text{GHz}}^{-(p-1)/2} \left(\frac{t_{\oplus,d}}{92(1+z)}\right)^{(21-15p)/10} \text{ mJy.} \quad (23)$$

Here, a factor of 0.8 is added to the expression to fit the late-time afterglow better. Figure 10 shows that the estimated energy using Eq. 23 is more accurate. Even at  $t \sim (1+z)t_{\text{SNT}}/2 \sim 100$  days, it only overestimates the energy by  $\sim 50\%$ . And the inferred energy using Eq. 23 agrees extremely well with the true energy after  $10^4$  days.

Fig. 7 shows that there is a bump in the lightcurves due to radiation from the counter jet. The late-time bump from the counter jet has been discussed by Granot & Loeb (2003); Li & Song (2004); Wang, Huang, & Kong (2009). However, the bump in our results is much smoother and broader than that in Granot & Loeb (2003); Li & Song (2004). Our results are consistent with those of Wang et al. (2009). Initially, the counter jet moves relativistically. Then it slows down and becomes nonrelativistic at  $t_{\text{NR}}$  in the lab frame. Its radiation cannot be observed by the observer on the earth until it becomes nonrelativistic at  $t_{\text{NR}}$  in the lab frame. This would lead to an estimate of the time for the counter jet bump in the lightcurve

$$t_{\text{cj},\oplus} \approx 2(1+z)t_{\text{NR}} \approx 1900(1+z)E_{\text{iso},53}^{1/3} n_0^{-1/3} \text{ days,} \quad (24)$$

and an estimate of the ratio of the two fluxes at the peak

$$\frac{F_{\nu,\text{cj}}}{F_{\nu,\text{fj}}} \approx \left(\frac{1}{3}\right)^{(21-15p)/10} \approx 6, \quad (25)$$

for  $p = 2.5$ . In our calculation of the afterglow lightcurves, for  $\nu_{\oplus} = 1$  GHz, the flux from the counter jet becomes comparable to that from the forward jet at  $\sim 1700$  days. At 3800 days, the ratio of the two fluxes at 1 GHz reaches its peak of 6. The above estimates (Eqs. 24 and 25) agree extremely well with the numerical results. Because  $t_{\text{NR}}$  is the nonrelativistic timescale in the lab frame for the fluid on the jet axis, it is expected that the first appearance of the counter jet bump from off-axis emission is earlier than  $t_{\text{cj},\oplus}$ . And numerical calculation indicates that the counter jet bump starts at  $\sim (1+z)t_{\text{NR}}$ .

#### 4. DISCUSSION

Our relativistic hydrodynamic simulation shows, as did Granot et al. (2001), that the sideways expansion of a relativistic GRB jet is a very slow process (§ 2.2). Analytic works (e.g., Rhoads 1999; Sari et al. 1999) based on a top-hat distribution of energy greatly overestimated the rate of the sideways expansion. A frequently asked question is, what is the speed of the sideways expansion? We think the question itself is wrong because it implicitly assumes a top-hat distribution during the expansion. This would always lead to an exponential growth of the jet opening angle. The jet during the expansion is indeed far from a top-hat distribution (Fig. 4), and it expands slowly. Another question is, what causes the jet break? Our calculations show that the jet break in GRB afterglow lightcurves is mainly caused by the *missing* flux when the edge of the jet is observed (§ 3.3.1). Fortunately, the widely used formula, Eq. 1 in Sari et al. (1999), which relates the jet break time to the properties of GRB jets is accurate.

It is generally believed that the spherical Sedov-von Neumann-Taylor self-similar solution can be applied at  $\sim t_{\text{NR}}$  (e.g., Piran 2005). We, however, find that the time  $t_{\text{NR}}$  is the beginning of a rather slow transition into the Sedov-von Neumann-Taylor solution, and the outflow at that time is still highly nonspherical (§ 2.2). Our simulation shows that the outflow can be described by the Sedov-von Neumann-Taylor solution after  $\sim 5t_{\text{NR}}$ . Note that the time  $t_{\text{NR}}$  measured in the lab frame is not equivalent to the observer time since the velocity of the flow is not sufficiently small yet compared with the speed of light. Fortunately again, the afterglow at  $t_{\oplus} \sim (1+z)t_{\text{NR}}$  is during the nonrelativistic phase.

We have found that the lightcurve after the jet break will become increasingly flatter over the time. But the flattening is a very gradual process. There is no characteristic timescale at which the lightcurve will suddenly become flatter. Our results disagree with the common notion that the flux density evolves as  $\propto t_{\oplus}^{-p}$  and then switches to  $\propto t_{\oplus}^{(21-15p)/10}$  after  $t_{\text{NR}}$  or  $t_s$ .

However, late-time radio observations can reveal a wealth of information about the GRB outflow. Eq. 23 can be potentially useful in determining the true energy of the outflow. We predict a late-time bump in flux density due to the radiation from the counter jet part of the outflow (see also Granot & Loeb 2003; Li & Song 2004; Wang et al. 2009). The radio afterglow of GRB 030329 had been observed up to 1128 days after the burst (van der Horst et al. 2008). No firm conclusion was drawn as to whether or not the emission from the counter jet had been observed. However, the counter jet bump may have been observed already in GRB 980703, which was monitored in the radio band up to  $\sim 1000$  days (Berger et al. 2001). It is reasonable to attribute the late-time radio flux to the host galaxy. However, it is also possible that the flux at  $\sim 1000$  days was actually emitted by the counter jet. This possibility could be easily tested through a future radio observation of the host galaxy of GRB 980703.

At the end of the hydrodynamic simulation ( $t \approx 150$  years), the GRB outflow is almost a sphere with an aspect ratio of  $\sim 0.8$ . Thus, it would be very difficult to distinguish such a GRB remnant at an age of more than  $\sim 200$  years from a supernova remnant using morphology alone. However, previous studies (Ayal & Piran 2001; Ramirez-Ruiz & MacFadyen 2008) have found that a GRB remnant in a similar interstellar medium will not become a sphere until  $\sim 5000$  years. The striking difference is due to different initial setups. In our hydrodynamic simulation, the GRB outflow initially moves

along the radial direction of spherical coordinates, whereas it moves parallel to the symmetric axis in their simulations. Obviously, the outflow sweeps up the surrounding medium at a much higher rate in our simulation than in theirs. Therefore, it is not surprising that the GRB outflow becomes a sphere at much earlier time in our simulation than in theirs.

High-resolution hydrodynamic simulations of GRB outflows are very computationally expensive. An intermediate approach to model the hydrodynamic evolution of GRB outflows could be as follows. A nonspreading jet obeying the Blandford-McKee solution can be assumed until  $t_{\text{NR}}$ . For  $t > 5t_{\text{NR}}$ , the outflow can be assumed to obey the Sedov-von Neumann-Taylor solution. Interpolation can be used for the transition phase  $t_{\text{NR}} < t < 5t_{\text{NR}}$  (see Fig. 5).

Many aspects of our numerical calculations can be improved. The calculation of radiation could include synchrotron self-absorption, which can be important for radio afterglow, and the inverse Compton process, which can be important for X-ray afterglow (Sari & Esin 2001; Harrison et al. 2001). In our numerical simulation, the hydrodynamic evolution of the GRB outflow is adiabatic. This is a good approximation provided that  $\epsilon_e \ll 1$  during the early fast cooling regime. However, radiative loss could greatly affect the hydrodynamics of the outflow during the early afterglow phase (e.g., less than a day) if  $\epsilon_e$  is close to 1 (Cohen, Piran, & Sari 1998).

A uniform jet described by the Blandford-McKee solution is assumed as the initial condition of our numerical simulation. This is justified because the jet initially moves at ultrarelativistic speeds and sideways expansion at very early times is likely to be modest. Besides uniform jet models based on the Blandford-McKee solution, structured jet models (Meszaros, Rees, & Wijers 1998; Perna, Sari, & Frail 2003; Granot & Kumar 2003) have also been proposed to explain various phenomena, including jet break (Dai & Gou 2001; Rossi, Lazzati, & Rees 2002; Zhang & Mészáros 2002). Moreover, numerical simulations have shown that nonuniform structures are expected for relativistic jets emerging from massive stars (Zhang, Woosley, & MacFadyen 2003; Zhang, Woosley, & Heger 2004; Morsony, Lazzati, & Begelman 2007). Recently Gruzinov (2007) has shown that the spherical Blandford-McKee solution is not an attractor for a generic asymmetric explosion. Therefore, it is very important to investigate non-Blandford-McKee models and their consequences on GRB afterglows with high-resolution numerical simulations, which we will present in future publications. We speculate that the shallow decay phase in the early X-ray afterglows of Swift bursts (e.g., Nousek et al. 2006; O’Brien et al. 2006) could be due to non-Blandford-McKee behavior of the outflow and the normal decay phase is reached as the outflow approaches the Blandford-McKee solution.

Magnetic field is not included in the two-dimensional relativistic hydrodynamic simulation presented in this paper, because we are mainly concerned with the stage when the magnetic field is no longer dynamically important. However, since GRB jets may be powered by electromagnetic processes (e.g., Blandford & Znajek 1977; Uzdensky & MacFadyen 2006, 2007; Barkov & Komissarov 2008; Bucciantini et al. 2009), magnetic field might have important effects on the dynamics of the jet during its pre-Blandford-McKee phase and early afterglows (e.g., Zhang & Kobayashi 2005). Preliminary one-dimensional relativistic magnetohydrodynamic simulations have found that the early afterglows are strong depen-

dent on the magnetization of the GRB outflow (Mimica et al. 2009).

The environment of a GRB can have a huge impact on its afterglow (e.g., Meszaros et al. 1998; Chevalier & Li 1999, 2000). Thus, another important issue is to investigate GRB outflows propagating in stellar winds since the progenitors of long soft GRBs are believed to be massive stars (Woosley 1993; Paczynski 1998; MacFadyen & Woosley 1999). More recently, late-time Chandra observations of the X-ray afterglow of GRB 060729 up to 642 days after the burst have been reported by Grupe et al. (2009). It is interesting that the lightcurve at such late times shows signs of steepening possibly due to either jet break or spectral break rather than flattening due to nonrelativistic motion. This might indicate that the onset of the Sedov-von Neumann-Taylor phase has been decayed due to the wind medium environment.

We adopted the standard approach in modeling GRB afterglow radiation. For example, the magnetic field is assumed to carry constant fractions of the internal energy density, and so do synchrotron emitting nonthermal relativistic electrons. Moreover, the fractions are assumed to be constant throughout the entire afterglow phase. The parameterization is a result of the lack of understanding of these processes. It remains unclear how magnetic fields are generated and how particles are accelerated in GRB outflows. The Weibel instability is a plausible mechanism (Gruzinov & Waxman 1999; Medvedev & Loeb 1999). Recent plasma simulations of the Weibel instability in relativistic collisionless shocks have shown promising results (Nishikawa et al. 2003; Spitkovsky 2008). More recently, Zhang, MacFadyen, & Wang (2009) have demonstrated amplification of magnetic field by a turbulent dynamo triggered by the Kelvin-Helmholtz instability with three-dimensional relativistic magnetohydrodynamic simulations. For conditions relevant for late afterglow and prompt GRB emission Zhang et al. (2009) obtained  $\epsilon_B \sim 5 \times 10^{-3}$ .

In this paper, we have calculated afterglows for an observer on the axis of the GRB jet. However, orphan afterglows are expected for an off-axis observer, who has missed the main burst because of the relativistic beaming effect (Rhoads 1997). The rate of orphan afterglows have been estimated analytically (Dalal et al. 2002; Granot et al. 2002; Levinson et al. 2002; Nakar et al. 2002). Thus far, no orphan afterglow has been detected. A recent survey of 68 local Type Ibc supernovae, including 6 broad-lines supernovae also known as “hypernovae” found no evidence of off-axis GRBs (Soderberg et al. 2006). Note that we have found that the sideways expansion has been overestimated in previous analytic works. Thus, previous analytic works tend to overestimate the rate of orphan afterglows. The issue of off-axis GRB afterglows will be investigated in a future publication.

We would like to thank Joseph Gelfand, Jonathan Granot, Andrei Gruzinov, Enrico Ramirez-Ruiz and Bing Zhang for many stimulating discussions. We appreciate helpful comments on the manuscript from Jonathan Granot and Bing Zhang. The RAM code used in this work was in part based upon the FLASH code developed by the DOE-supported ASCI/Alliance Center for Astrophysical Thermonuclear Flashes at the University of Chicago. Specifically, we used the PARAMESH AMR and I/O tools from FLASH version 2.3.

## REFERENCES

- Ayal, S., & Piran, T. 2001, *ApJ*, 555, 23
- Barkov, M. V., & Komissarov, S. S. 2008, *MNRAS*, 385, L28
- Berger, E., Kulkarni, S. R., & Frail, D. A. 2001, *ApJ*, 560, 652  
—, 2004, *ApJ*, 612, 966
- Blandford, R. D., & McKee, C. F. 1976, *Physics of Fluids*, 19, 1130
- Blandford, R. D., & Znajek, R. L. 1977, *MNRAS*, 179, 433
- Bucciantini, N., Quataert, E., Metzger, B. D., Thompson, T. A., Arons, J., & Del Zanna, L. 2009, *MNRAS*, submitted, arXiv:0901.3801
- Cannizzo, J. K., Gehrels, N., & Vishniac, E. T. 2004, *ApJ*, 601, 380
- Chevalier, R. A., & Li, Z.-Y. 1999, *ApJ*, 520, L29  
—, 2000, *ApJ*, 536, 195
- Cohen, E., Piran, T., & Sari, R. 1998, *ApJ*, 509, 717
- Dai, Z. G., & Gou, L. J. 2001, *ApJ*, 552, 72
- Dai, Z. G., & Lu, T. 1999, *ApJ*, 519, L155
- Dalal, N., Griest, K., & Pruet, J. 2002, *ApJ*, 564, 209
- Frail, D. A., Kulkarni, S. R., Sari, R., Djorgovski, S. G., Bloom, J. S., Galama, T. J., Reichart, D. E., Berger, E., Harrison, F. A., Price, P. A., Yost, S. A., Diercks, A., Goodrich, R. W., & Chaffee, F. 2001, *ApJ*, 562, L55
- Frail, D. A., Soderberg, A. M., Kulkarni, S. R., Berger, E., Yost, S., Fox, D. W., & Harrison, F. A. 2005, *ApJ*, 619, 994
- Frail, D. A., Waxman, E., & Kulkarni, S. R. 2000, *ApJ*, 537, 191
- Fryxell, B., Olson, K., Ricker, P., Timmes, F. X., Zingale, M., Lamb, D. Q., MacNeice, P., Rosner, R., Truran, J. W., & Tufo, H. 2000, *ApJS*, 131, 273
- Granot, J. 2007, in *Revista Mexicana de Astronomía y Astrofísica Conference Series*, Vol. 27, *Revista Mexicana de Astronomía y Astrofísica*, vol. 27, 140–165
- Granot, J., & Kumar, P. 2003, *ApJ*, 591, 1086
- Granot, J., & Loeb, A. 2003, *ApJ*, 593, L81
- Granot, J., Miller, M., Piran, T., Suen, W. M., & Hughes, P. A. 2001, in *Gamma-ray Bursts in the Afterglow Era*, ed. E. Costa, F. Frontera, & J. Hjorth, 312
- Granot, J., Panaitescu, A., Kumar, P., & Woosley, S. E. 2002, *ApJ*, 570, L61
- Granot, J., Piran, T., & Sari, R. 1999, *ApJ*, 513, 679
- Grupe, D., Burrows, D. N., Xue-Feng, Wang, X.-Y., Zhang, B., Garmire, G., Nousek, J. A., Gehrels, N., Ricker, G., & Bautz, M. W. 2009, *ApJ*, submitted, arXiv:0903.1258
- Gruzinov, A. 2007, arXiv:0704.3081
- Gruzinov, A., & Waxman, E. 1999, *ApJ*, 511, 852
- Harrison, F. A., Bloom, J. S., Frail, D. A., Sari, R., Kulkarni, S. R., Djorgovski, S. G., Axelrod, T., Mould, J., Schmidt, B. P., Wieringa, M. H., Wark, R. M., Subrahmanyan, R., McConnell, D., McCarthy, P. J., Schaefer, B. E., McMahon, R. G., Markze, R. O., Firth, E., Soffitta, P., & Amati, L. 1999, *ApJ*, 523, L121
- Harrison, F. A., Yost, S. A., Sari, R., Berger, E., Galama, T. J., Holtzman, J., Axelrod, T., Bloom, J. S., Chevalier, R., Costa, E., Diercks, A., Djorgovski, S. G., Frail, D. A., Frontera, F., Hurlley, K., Kulkarni, S. R., McCarthy, P., Piro, L., Pooley, G. G., Price, P. A., Reichart, D., Ricker, G. R., Shepherd, D., Schmidt, B., Walter, F., & Wheeler, C. 2001, *ApJ*, 559, 123
- Huang, Y. F., & Cheng, K. S. 2003, *MNRAS*, 341, 263
- Kumar, P., & Granot, J. 2003, *ApJ*, 591, 1075
- Levinson, A., Ofek, E. O., Waxman, E., & Gal-Yam, A. 2002, *ApJ*, 576, 923
- Li, Z., & Song, L. M. 2004, *ApJ*, 614, L17
- Livio, M., & Waxman, E. 2000, *ApJ*, 538, 187
- MacFadyen, A. I., & Woosley, S. E. 1999, *ApJ*, 524, 262
- MacNeice, P., Olson, K. M., Mobarry, C., de Fainchtein, R., & Packer, C. 2000, *Computer Physics Communications*, 126, 330
- Medvedev, M. V., & Loeb, A. 1999, *ApJ*, 526, 697
- Meszáros, P. 2006, *Reports on Progress in Physics*, 69, 2259
- Meszáros, P., & Rees, M. J. 1997, *ApJ*, 476, 232
- Mészáros, P., & Rees, M. J. 1999, *MNRAS*, 306, L39
- Meszáros, P., Rees, M. J., & Wijers, R. A. M. J. 1998, *ApJ*, 499, 301
- Mignone, A., Plewa, T., & Bodo, G. 2005, *ApJS*, 160, 199
- Mimica, P., Giannios, D., & Aloy, M. A. 2009, *A&A*, 494, 879
- Morsony, B. J., Lazzati, D., & Begelman, M. C. 2007, *ApJ*, 665, 569
- Nakar, E., Piran, T., & Granot, J. 2002, *ApJ*, 579, 699
- Nishikawa, K.-I., Hardee, P., Richardson, G., Preece, R., Sol, H., & Fishman, G. J. 2003, *ApJ*, 595, 555
- Nousek, J. A., Kouveliotou, C., Grupe, D., Page, K. L., Granot, J., Ramirez-Ruiz, E., Patel, S. K., Burrows, D. N., Mangano, V., Barthelmy, S., Beardmore, A. P., Campana, S., Capalbi, M., Chincarini, G., Cusumano, G., Falcone, A. D., Gehrels, N., Giommi, P., Goad, M. R., Godet, O., Hurkett, C. P., Kennea, J. A., Moretti, A., O'Brien, P. T., Osborne, J. P., Romano, P., Tagliaferri, G., & Wells, A. A. 2006, *ApJ*, 642, 389
- O'Brien, P. T., Willingale, R., Osborne, J., Goad, M. R., Page, K. L., Vaughan, S., Rol, E., Beardmore, A., Godet, O., Hurkett, C. P., Wells, A., Zhang, B., Kobayashi, S., Burrows, D. N., Nousek, J. A., Kennea, J. A., Falcone, A., Grupe, D., Gehrels, N., Barthelmy, S., Cannizzo, J., Cummings, J., Hill, J. E., Krimm, H., Chincarini, G., Tagliaferri, G., Campana, S., Moretti, A., Giommi, P., Perri, M., Mangano, V., & LaParola, V. 2006, *ApJ*, 647, 1213
- Paczynski, B. 1998, *ApJ*, 494, L45
- Panaitescu, A., & Kumar, P. 2001, *ApJ*, 560, L49  
—, 2002, *ApJ*, 571, 779
- Panaitescu, A., & Mészáros, P. 1999, *ApJ*, 526, 707
- Perna, R., Sari, R., & Frail, D. 2003, *ApJ*, 594, 379
- Piran, T. 2005, *Reviews of Modern Physics*, 76, 1143
- Ramirez-Ruiz, E., & MacFadyen, A. I. 2008, *ApJ*, submitted, arXiv:0808.3448
- Rhoads, J. E. 1997, *ApJ*, 487, L1  
—, 1999, *ApJ*, 525, 737
- Rossi, E., Lazzati, D., & Rees, M. J. 2002, *MNRAS*, 332, 945
- Sari, R., & Esin, A. A. 2001, *ApJ*, 548, 787
- Sari, R., Piran, T., & Halpern, J. P. 1999, *ApJ*, 519, L17
- Sari, R., Piran, T., & Narayan, R. 1998, *ApJ*, 497, L17
- Soderberg, A. M., Nakar, E., Berger, E., & Kulkarni, S. R. 2006, *ApJ*, 638, 930
- Spitkovsky, A. 2008, *ApJ*, 682, L5
- Stanek, K. Z., Garnavich, P. M., Kaluzny, J., Pych, W., & Thompson, I. 1999, *ApJ*, 522, L39
- Syngé, J. L. 1971, *The Relativistic Gas* (Amsterdam: North-Holland)
- Uzdensky, D. A., & MacFadyen, A. I. 2006, *ApJ*, 647, 1192  
—, 2007, *ApJ*, 669, 546
- van der Horst, A. J., Kamble, A., Resmi, L., Wijers, R. A. M. J., Bhattacharya, D., Scheers, B., Rol, E., Strom, R., Kouveliotou, C., Oosterloo, T., & Ishwara-Chandra, C. H. 2008, *A&A*, 480, 35
- Wang, X., Huang, Y. F., & Kong, S.-W. 2009, *A&A*, submitted, arXiv:0903.3119
- Waxman, E. 1997a, *ApJ*, 489, L33  
—, 1997b, *ApJ*, 485, L5
- Wijers, R. A. M. J., Rees, M. J., & Meszaros, P. 1997, *MNRAS*, 288, L51
- Woosley, S. E. 1993, *ApJ*, 405, 273
- Zeh, A., Klose, S., & Kann, D. A. 2006, *ApJ*, 637, 889
- Zhang, B., & Kobayashi, S. 2005, *ApJ*, 628, 315
- Zhang, B., & Mészáros, P. 2002, *ApJ*, 571, 876  
—, 2004, *International Journal of Modern Physics A*, 19, 2385
- Zhang, W., MacFadyen, A., & Wang, P. 2009, *ApJ*, 692, L40
- Zhang, W., & MacFadyen, A. I. 2006, *ApJS*, 164, 255
- Zhang, W., Woosley, S. E., & Heger, A. 2004, *ApJ*, 608, 365
- Zhang, W., Woosley, S. E., & MacFadyen, A. I. 2003, *ApJ*, 586, 356